AStA Adv Stat Anal (2009) 93: 237–261
DOI 10.1007/s10182-009-0106-5

ORIGINAL PAPER

Anisotropy analysis of pressed point processes

**Claudia Redenbach · Aila Särkkä ·
Johannes Freitag · Katja Schladitz**

Received: 15 July 2008 / Accepted: 6 January 2009 / Published online: 13 February 2009

Abstract This paper introduces methods for the detection of anisotropies which are caused by compression of regular 3D point patterns. Isotropy tests based on directional summary statistics and estimators for the compression factor are developed. Using simulated data, the dependence of the power of these methods on the intensity, the degree of regularity, and the compression strength is studied. Finally, our methods are applied to the point patterns of centers of air pores extracted from tomographic images of ice cores. This way the presence of anisotropies in the ice caused by the compression of the ice sheet and an increase of their strength with increasing depth are shown.

This work is a contribution to the Talos Dome Ice core Project (TALDICE), a joint European programme, funded by national contributions from Italy, France, Germany, Switzerland, and the United Kingdom. The main logistic support was provided by PNRA. This is TALDICE publication no. 3.

C. Redenbach (✉)
University of Applied Sciences Darmstadt and Fraunhofer Institute for Industrial Mathematics (ITWM), Fraunhofer-Platz 1, 67663 Kaiserslautern, Germany
e-mail: claudia.redenbach@itwm.fraunhofer.de

A. Särkkä
Department of Mathematical Sciences, Chalmers University of Technology, Gothenburg, Sweden

A. Särkkä
Department of Mathematical Sciences, University of Gothenburg, 41296 Gothenburg, Sweden

J. Freitag
Alfred Wegener Institute for Polar and Marine Research, Columbusstraße, 27568 Bremerhaven, Germany

K. Schladitz
Fraunhofer Institute for Industrial Mathematics (ITWM), Fraunhofer-Platz 1, 67663 Kaiserslautern, Germany

Keywords Estimation of compression · Isotropy test · Nearest neighbor distance · Orientation analysis · Ripley's K function

1 Introduction

Polar ice is a remarkable multi-proxy archive for climate information of the past. With the perspective of highly resolved time series over hundreds of thousand years, it has attracted considerable interest of climate researchers. During the last decades, a couple of deep polar ice cores were drilled through the Antarctic and Greenlandic ice sheets. Several proxy parameters are identified in the ice, e.g., temperature, precipitation, dust, aerosol, sea ice extent, biological activity, and atmospheric composition including the famous records of trace and greenhouse gases (Bender et al. 1994; EPICA community members 2004; EPICA community members 2006). Accurate chronologies are an important requirement for the interpretation of ice core records. However, they are not satisfyingly developed until now. No absolute dating tool is available for polar ice. The recent dating relies on models. Their key element is the simulation of the individual history of ice deformation for each specific core site. In this paper we present the first direct method for the estimation of the deformation history (expressed by the thinning function as explained below) in polar ice using the measured anisotropy of air inclusions in centimeter-sized ice samples from a deep ice core.

An idealized ice sheet consists of a vertical sequence of compressed snow layers that have been buried under the load of newly fallen snow. Because ice under pressure is subject to creep, there is a vertical compression accompanied by a total lateral transport of ice from the interior of an ice sheet to its boundaries. At the boundaries the ice is exported to the ocean via iceberg calving and melting. Due to the interaction of compression and lateral transport, the pore structures at different compression rates do not differ significantly at first sight. In particular, counterintuitively the number of pores per volume does not increase considerably owing to the incompressibility of the ice. Furthermore, even ice samples taken from the same depth show a high variability in their pore structure by reason of seasonal variations and the small sample size. CT imaging can only handle centimeter-sized samples, while the compression rates vary on scales of 10 meters. The key question is therefore, whether the compression rate can be deduced from the pore structure.

The age of an ice layer is defined as the time when the water molecules of such a layer have been accumulated on the surface of the ice sheet as snow. At undisturbed sites the age is continuously increasing with depth with the oldest ice at the bottom. The oldest ice drilled so far is dated back to about 100 000 years in Greenland (Summit station, 72°34′ N, 37°37′ W, GRIP ice core) and to about 800 000 years in Antarctica (Dome Concordia station, 75°06′ S, 123°20′ E, EPICA-EDC ice core). Flow models that are used for dating describe the thinning of annual layers with depth based on a mechanical model and on assumptions about bedrock conditions and surface elevation changes in the past (Paterson 1994; Parrenin et al. 2007; Ruth et al. 2007; Severi et al. 2007). Then the derived thinning function is combined with a snow accumulation model for the past to estimate the age of the ice as a function of depth. Diverse input parameters of such models are not well constrained including the mechanical properties of polycrystalline ice with different chemical load and crystal orientation (a topic of growing interest which is not fully understood, Duval 2000) with consequences for the formulation of the constitutive law in the mechanical model. Due to the complex interaction between bedrock and ice, it will also be difficult to formulate a physical model for the flow conditions at the bedrock boundary. Parrenin et al. (2007) tried to avoid these problems in the model parametrizations by the application of an inverse method using some fixed absolute age markers in the core.

In this paper we show that the total thinning in polar ice could be directly retrieved from measured air inclusions in combination with a statistical method analyzing pressed point processes. We have chosen unmarked summary statistics because the anisotropy cannot be seen in the shape of the pores, which are more or less spherical on the deeper layers. The definition of the summary statistics is similar to some statistics which have been used in two-dimensional applications. However, in order to apply these statistics in a three-dimensional setting, a variety of technical problems have to be overcome. We believe that this is the first application of the summary statistics K and G, well known from spatial statistics, to anisotropic 3D data. In our first attempt the application is restricted to samples from an ice core drilled at a Dome position where the acting forces are known. In the case of a Dome one can assume that ice deforms simply in uniaxial compression. Ice layers are compressed by a factor of c in the vertical and stretched in the lateral direction by a factor of $1/\sqrt{c}$ keeping the total volume constant. The factor c gives the total thinning of an ice layer. The bubble-like air inclusions inside the ice matrix are used as strain markers. They are relicts of a long-term sintering process in the firn column. The term firn refers to the upper 50 to 100 m of an ice sheet and describes sintered ice grains with connected air-filled pores in between. The ice grains form an ensemble of tetrakaidecahedrons with the air located at their edges. At the firn–ice transition the interconnected pore space starts to isolate in individual bubbles. Firn becomes ice per definition. During the sintering and compaction, the pore volume is continuously decreasing from 50% to about 10% of the total volume at the firn–ice transition. The close-off process results in a quite regular and uniform distribution of bubbles within the ice. Their regularity originates from the initial homogeneity of surface snow and the moderate sintering conditions, particularly the long sintering time with only slowly increasing pressure load. The mean distance between adjacent bubbles is of the order of the grain size and this is about 1 mm at the firn–ice transition. Below the firn–ice transition the bubble distributions are only affected by the overall deformation process of the ice itself. Bubble migration due to further grain growth or small temperature gradients is negligible. The increasing pressure with depth leads to bubble shrinkage but again without affecting the distribution of the bubble centers. At pressure loads below about 600 to 700 m depth the bubbles become unstable, and the enclosed air is captured as clathrates in the ice. There is a natural depth limit for the existence of bubbles in polar ice and therefore for the application of our method to deep polar ice cores.

The paper is organized as follows. First, we introduce some directional summary statistics in 3D, which are then used as the basis for some isotropy tests. The tests are constructed in order to reveal the particular type of anisotropy caused by simultaneous compression and lateral transport. In Sect. 4 we perform a simulation study comparing the powers of the tests based on different summary statistics. The estimation of the pressing factor is discussed in Sect. 5. Both studies are performed on a more general level than needed for the analysis of the ice samples in order to explore the range of applicability of the suggested methods. Finally, the methods are applied to the air pore data. The anisotropy of air pores is studied, and the pressing factors are estimated at different depths.

2 Directional summary statistics

There are several summary statistics which can be used to study the spatial distribution of a point pattern. The nearest-neighbor distance distribution function G is the distribution function of the distance from a typical point of the process to its nearest neighbor. The empty space function F is the distribution of distance to the nearest point of the process from a random point in space. The J function is a combination of the G and F functions. Finally, Ripley's K function is related to the expected number of further points of the process within a certain distance from a typical point of the point process, and the pair-correlation function g is essentially the derivative of the K function w.r.t. the distance (for all these functions, see, e.g., Diggle 2003). Originally, these functions have been defined in 2D but they can be defined exactly in the same way for three-dimensional point processes. Usually, these statistics assume that the point pattern is a realization of a stationary and isotropic point process.

Here, we are interested in detecting possible anisotropies which requires directional counterparts of these functions. So far, this problem has only been studied in the 2D case. Stoyan and Beneš (1991) discuss different types of anisotropies in marked point patterns, namely anisotropies of marks (orientation of marks) and anisotropic distribution of points. They define the point-pair rose density, which describes the anisotropy of the arrangement of points, possibly including information on the marks. The idea is as follows. Choose a pair of points with distance in a certain interval (r_1, r_2) at random and determine the angle β between the line going through the points and the 0-direction. This angle is a random variable taking values between 0 and π, whose distribution gives information on the arrangement of the points. The point-pair rose density $o_{r_1 r_2}(\beta)$ is the corresponding probability density function (weighted by the marks). It is an integrated version of the anisotropic pair-correlation function, which is defined as follows (Stoyan 1991). The second-order product density $\varrho(x_1, x_2)$ is related to the probability of finding points of the process in small neighborhoods of both x_1 and x_2. In the stationary but anisotropic case, ϱ is a function of the distance r and the angle φ between the line going through x_1 and x_2 and the 0-direction. The anisotropic pair correlation function is then $g(r, \varphi) = \varrho(r, \varphi)/\lambda^2$, where λ is the intensity of the point process. Both for the point-pair rose density and the anisotropic pair-correlation function, an edge-corrected kernel estimator should be used. Furthermore, Stoyan et al. (1995, p. 127) define a directional version of Ripley's K function.

The definitions of these functions carry over to the 3D case without any difficulties. However, the practical evaluation and the visualization of the results becomes more challenging. Already in 2D, directional summary statistics depend on two variables, the distance and the angle. Nevertheless, it is obvious how to divide a disc into sectors of equal size such that the summary statistics can be estimated for a discrete set of parameters. Circular diagrams or plots over the interval $[0, 2\pi]$ can then be used to display the results.

In 3D, three variables, the distance and two angles, have to be used. The estimation of the directional summary statistics with respect to different directions requires a suitable partition of the ball. The sectors should be of equal size and shape, which means that the directions should be distributed as uniformly as possible. Other choices might hold the danger of introducing some structure in the results which is caused by the partitioning of the ball rather than by the data. In general, it is not clear how to choose such a partition in a way that it is easily parametrized, e.g., by means of spherical coordinates.

Here, we are dealing with a special type of anisotropy, namely anisotropy in z-direction caused by compression of the point process. In this case, the behavior of the point process in z-direction has to be compared to other reference directions, e.g., the x- and y-direction. For this purpose, the process has to be studied within suitable sets aligned along these directions. A complete partitioning of the ball is not necessarily required.

One type of ball segments which are described easily in spherical coordinates, and therefore suitable for our application, are spherical cones. Let $C_u(r,\theta)$ with $r \geq 0$ and $0 \leq \theta \leq \pi$ denote the double spherical cone defined as

$$C_u(r,\theta) = \left\{ R_u \begin{pmatrix} s \sin\vartheta \cos\varphi \\ s \sin\vartheta \sin\varphi \\ s \cos\vartheta \end{pmatrix} : s \in [0,r], \vartheta \in [0,\theta] \cap [\pi-\theta,\pi], \varphi \in [0,2\pi] \right\},$$

where u is a unit vector, and R_u is a rotation mapping the z-axis on the line spanned by u. In order to detect anisotropies, the point pattern is observed within three double cones aligned along the coordinate axes and centered in the typical point of the process. A compressed point process will have a different appearance within the z-cone than within the x- and y-cones.

In the following we define the directional summary statistics which will be used to detect the anisotropies. Already Stoyan et al. (1995, p. 153) discuss how to use the directional K function and its zero-contours to estimate the pressing factor of pressed point patterns. Therefore, the directional K function is the first function to be considered here. The density functions mentioned above, namely the point-pair rose density and the anisotropic pair-correlation function, are good when investigating and describing anisotropies in a particular point pattern. However, these functions are usually estimated by using kernel estimators. In addition to the technical problems in 3D, an analysis based on these functions would therefore pose further questions such as the choice of a suitable bandwidth. For testing and estimation purposes it might be a better idea to use cumulative functions like the directional K function. Smaller local fluctuations in the cumulative functions should make the comparison of the results for different directions more stable. In addition to the directional K function, we will therefore consider two directional counterparts of the nearest-neighbor distance distribution function G.

2.1 Directional K function K_{dir}

We consider a directional version of Ripley's K-function, namely the second reduced moment measure of the cone $C_u(r,\theta)$, which is denoted by $K_{\text{dir},u,\theta}(r)$. This means that $K_{\text{dir},u,\theta}(r)$ is the expected number of points within the double cone centered in a typical point of the point process Ψ. An unbiased estimator of $\lambda^2 K_{\text{dir},u}(r)$ is given by

$$\lambda^2 \hat{K}_{\text{dir},u,\theta}(r) = \sum_{x\in\Psi} \sum_{y\in\Psi, y\neq x} \frac{\mathbb{1}_{C_u(r,\theta)}(x-y)}{|W_x \cap W_y|}, \quad r \geq 0, \tag{1}$$

where W_x is the translation of the window W by the vector x, and $|B|$ denotes the volume of a set $B \subset \mathbb{R}^3$ (Stoyan et al. 1995, p. 134 f).

2.2 Directional G functions

Pressing a hard core point pattern will transform the empty ball centered in each point of the process into an ellipsoid. Therefore, this particular kind of anisotropy will influence the distribution of the distance to the nearest neighbor. The nearest neighbor in z-direction will be closer than the nearest neighbor in x- or y-direction. Depending on whether the nearest neighbor is determined locally or globally, this gives rise to the following summary statistics:

2.2.1 Local G function G_{loc}

Here, the nearest neighbor is defined locally, i.e., we are looking for the nearest neighbor contained in the cone $x + C_u(r,\theta)$ centered in a point $x \in \Psi$. Denote by $G_{\text{loc},u,\theta}$ the distribution function of the distance from the typical point of the process to the closest point in the cone. In order to define an estimator for $G_{\text{loc},u,\theta}$, let Ψ' denote the point process of points $x \in \Psi$ marked with the distance d to the closest point in $x + C_u(r,\theta)$ and consider the distribution of the distance d. We use the Hanisch-type estimator for $G_{\text{loc},u,\theta}$ given by

$$\hat{G}_{\text{loc},u,\theta}(r) = \frac{\hat{G}_{H,\text{loc},u,\theta}(r)}{\hat{\lambda}_H} \tag{2}$$

with

$$\hat{G}_{H,\text{loc},u,\theta}(r) = \sum_{(x,d)\in\Psi'} \frac{\mathbb{1}_{[0,r]}(d)\,\mathbb{1}_{W\ominus C_u(d,\theta)}(x)}{|W \ominus C_u(d,\theta)|}, \quad r \geq 0,$$

and

$$\hat{\lambda}_H = \sum_{(x,d)\in\Psi'} \frac{\mathbb{1}_{W\ominus C_u(d,\theta)}(x)}{|W \ominus C_u(d,\theta)|}.$$

The term $W \ominus C_u(d,\theta)$ denotes the erosion of the window W by the cone $C_u(d,\theta)$ and is included for edge correction. We consider only those points $x \in \Psi$ with the property that the complete cone $x + C_u(d,\theta)$ is contained in the observation window W. As in Hanisch (1984), it can be shown that $\hat{G}_{H,\text{loc},u,\theta}$ is an unbiased estimator for $\lambda G_{\text{loc},u,\theta}$.

2.2.2 *Global G function G_{glob}*

In this case we determine the global nearest neighbor $y \in \Psi$ for each point $x \in \Psi$ and denote the marked point process of pairs (x, y) by Ψ'. Then, $G_{\text{glob},u,\theta}$ is defined as the distribution function of the distance between x and y conditioned on $y \in x + C_u(r, \theta)$. An estimator for $G_{\text{glob},u,\theta}(r, \theta)$ is then given by

$$\hat{G}_{\text{glob},u,\theta}(r) = \frac{\sum_{(x,y)\in\Psi'} \mathbb{1}_{C_u(r,\theta)}(x-y)\, \mathbb{1}_{W\ominus b(0,\|x-y\|)}(x)}{\sum_{(x,y)\in\Psi'} \mathbb{1}_{C_u(\infty,\theta)}(x-y)\, \mathbb{1}_{W\ominus b(0,\|x-y\|)}(x)}, \quad r \geq 0. \tag{3}$$

Here, we consider only the points $x \in \Psi$ with the property that the ball $b(x, \|x - y\|)$ is completely contained in W.

Compared to G_{loc}, the global G function depends on a smaller number of points of Ψ. Therefore, G_{loc} should yield better results for small intensities, while, being related to the nearest-neighbor orientation density, G_{glob} might be a good alternative in the case of high-intensity patterns. A drawback of the G functions might be their "short-sightedness" caused by the consideration of only nearest neighbors (Illian et al. 2008, p. 214). Even though the phenomena we are studying are rather local, the use of second-order methods such as K_{dir} might be expected to yield better results.

3 Isotropy tests

In the following, we introduce some tests which seem suitable to detect anisotropies caused by pressing of isotropic hard core point processes. Monte Carlo tests are very common tests in spatial statistics (Stoyan and Stoyan 1994). This technique, however, requires an appropriate model for the data under investigation. Deviations between the model and the data might then result in a loss of power of the related tests. Since we are working with replicated data, we will therefore concentrate on nonparametric methods which are only based on estimations from the data and do not require further simulations.

3.1 Tests using summary statistics

Let $\hat{S}_x$, $\hat{S}_y$, and $\hat{S}_z$ be estimators of one of the summary statistics introduced above with respect to the x-, y-, and z-direction. In the isotropic case, all three estimates will look similar. For the pressed pattern, only $\hat{S}_x$ and $\hat{S}_y$ should be similar but show a clear deviation from $\hat{S}_z$.

Consider n point patterns $\psi_1, \ldots, \psi_n$ which can be assumed to have the same distribution and should be tested for isotropy. If the number of samples n is large, a test can be based on a comparison of the test statistics

$$T_{xy,i} = \int_{r_1}^{r_2} \left|\hat{S}_{x,i}(r) - \hat{S}_{y,i}(r)\right| dr, \quad i = 1, \ldots, n,$$

and

$$T_{z,i} = \min\left(\int_{r_1}^{r_2} \left|\hat{S}_{x,i}(r) - \hat{S}_{z,i}(r)\right| dr, \int_{r_1}^{r_2} \left|\hat{S}_{y,i}(r) - \hat{S}_{z,i}(r)\right| dr\right), \quad i = 1, \ldots, n,$$

where $[r_1, r_2]$ is a given interval. T_z is defined using the minimum to make sure that the z-direction differs from both the x- and the y-direction. Other choices such as the mean or the maximum could be considered as well. The isotropy hypothesis for a certain sample ψ_i is rejected at significance level α if the corresponding value $T_{z,i}$ is larger than $100(1-\alpha)\%$ of the estimated T_{xy} values.

If only a few samples are available, a Monte Carlo test using the test statistic

$$T_{\sum} = \int_{r_1}^{r_2} \left(\left|\hat{S}_x(r) - \hat{S}_y(r)\right| + \left|\hat{S}_y(r) - \hat{S}_z(r)\right| + \left|\hat{S}_z(r) - \hat{S}_x(r)\right|\right) dr$$

can be considered alternatively. This test, however, requires the existence and the simulation of an appropriate model for the data. Under an isotropic model, in theory all three functions S_x, S_y, and S_z are equal, hence $T_{\sum} = 0$.

The alternative statistics

$$T'_{xy} = \max_{r_1 \le r \le r_2} \left|\hat{S}_x(r) - \hat{S}_y(r)\right|,$$

$$T'_z = \min\left(\max_{r_1 \le r \le r_2} \left|\hat{S}_x(r) - \hat{S}_z(r)\right|, \max_{r_1 \le r \le r_2} \left|\hat{S}_y(r) - \hat{S}_z(r)\right|\right),$$

and

$$T'_{\sum} = \max_{r_1 \le r \le r_2} \left(\left|\hat{S}_x(r) - \hat{S}_y(r)\right| + \left|\hat{S}_y(r) - \hat{S}_z(r)\right| + \left|\hat{S}_z(r) - \hat{S}_x(r)\right|\right)$$

were also considered in first trials but performed worse than the integral statistics above due to large local differences between the functions $\hat{S}_x$, $\hat{S}_y$, and $\hat{S}_z$.

3.2 Direction to the nearest neighbor

The compression of a hard core point process will result in a pattern where the points are closer in z-direction than they are in x- or y-direction. Therefore, the direction to the nearest neighbor after pressing will have a preferred direction along the z-axis. As an alternative to the tests using directional summary statistics, we test this directional distribution for uniformity against the alternative of a preferred direction using the test described in Anderson and Stephens (1972). This provides us with another model-free method, whose advantage is its simplicity. It only requires the computation of the directions to the nearest neighbors, a further choice of parameters such as the interval $[r_1, r_2]$ or the size of the cone is not necessary. However, looking only at directions, rather than directions and distances, this test might be less powerful than tests based on both quantities.

The uniformity test works as follows. Suppose that a set of unit vectors $v_i = (x_i, y_i, z_i)$, $i = 1, \ldots, n$, is given. Then compute the orientation matrix

$$A = \begin{pmatrix} \sum x_i^2 & \sum x_i y_i & \sum x_i z_i \\ \sum x_i y_i & \sum y_i^2 & \sum y_i z_i \\ \sum x_i z_i & \sum y_i z_i & \sum z_i^2 \end{pmatrix}.$$

Denote the eigenvalues of A by $\lambda_1 \geq \lambda_2 \geq \lambda_3$ and the corresponding eigenvectors by u_1, u_2, and u_3. The value of λ_1 is used as a test statistic for the uniformity test against a bimodal alternative. If λ_1 is too large, the uniformity hypothesis is rejected, and u_1 yields a maximum likelihood estimate of the modal vector. For $n > 100$, the significance points for λ_1 at a 5% significance level are given by $\frac{1}{3} + \frac{0.873}{\sqrt{n}}$.

4 Simulations

In the following, we will evaluate the powers of the anisotropy tests introduced above applying them to simulated data. We believe that our methods could be applied to both clustered and regular point patterns. Nevertheless we restrict ourselves to hard core point processes since the air pore structures are regular. In order to cover a wide range of such patterns, we are going to study two established models: a Matérn hard core point process and a random packing of balls with a much higher degree of regularity. The choice of the parameter values in the simulations (intensity, hard core radius) is motivated by the values in the ice data. Isotropic realizations of both models are scaled by the vector $(\frac{1}{\sqrt{c}}, \frac{1}{\sqrt{c}}, c)$ with $0 < c \leq 1$. This means that the patterns are compressed in z-direction but stretched in x- and y-direction so that the volume of the observation window is preserved. For the estimation of the summary statistics, the value $\theta = \frac{\pi}{4}$ was chosen, which yields reasonably large but still nonoverlapping cones.

4.1 Matérn hard core point process

Realizations of Matérn hard core point processes with intensities $\lambda = 500$ and hard core radius $R = 0.025, 0.05$, and 0.075 as well as $\lambda = 1000$ and $R = 0.025$ and 0.05 were simulated. The isotropic realizations were generated within the cuboids $[0, \sqrt{c}] \times [0, \sqrt{c}] \times [0, \frac{1}{c}]$ with $c = 0.7, 0.8$, and 0.9. The pressing of these realizations with the factor c then yielded point patterns within the unit cube. For each set of parameters, we simulated 1000 realizations of the pressed point patterns. Each of these realizations was tested for isotropy using the tests based on $G_{\mathrm{loc}}, G_{\mathrm{glob}}$, and K_{dir}. In order to keep the extend of the paper limited, only the results for $\lambda = 500$ are presented here.

Good results of the estimation can only be expected if the envelopes of the directional summary statistics do not overlap too much on the chosen observation interval. For the largest hard core values considered, this is the case on the interval $[0, 1.1R]$, which was therefore chosen for the computation of the test statistics (see also Fig. 1). In order to check the dependence of the test results on the choice of the interval, the alternatives $[0, \frac{4R}{3}]$ and $[0, 0.1]$ ($[0, 0.1]$ and $[0, 0.2]$ for $R = 0.075$) were also considered. For $\lambda = 500$, the powers of these tests and the uniformity test for the direction to the nearest neighbor based on the eigenvalue λ_1 are given in Table 1. The powers obtained for $\lambda = 1000$ show a similar behavior but tend to be higher than those for $\lambda = 500$.

As expected, higher powers are achieved for higher intensities, larger hard core radii, and stronger pressing. In all cases, the best results were obtained on the interval

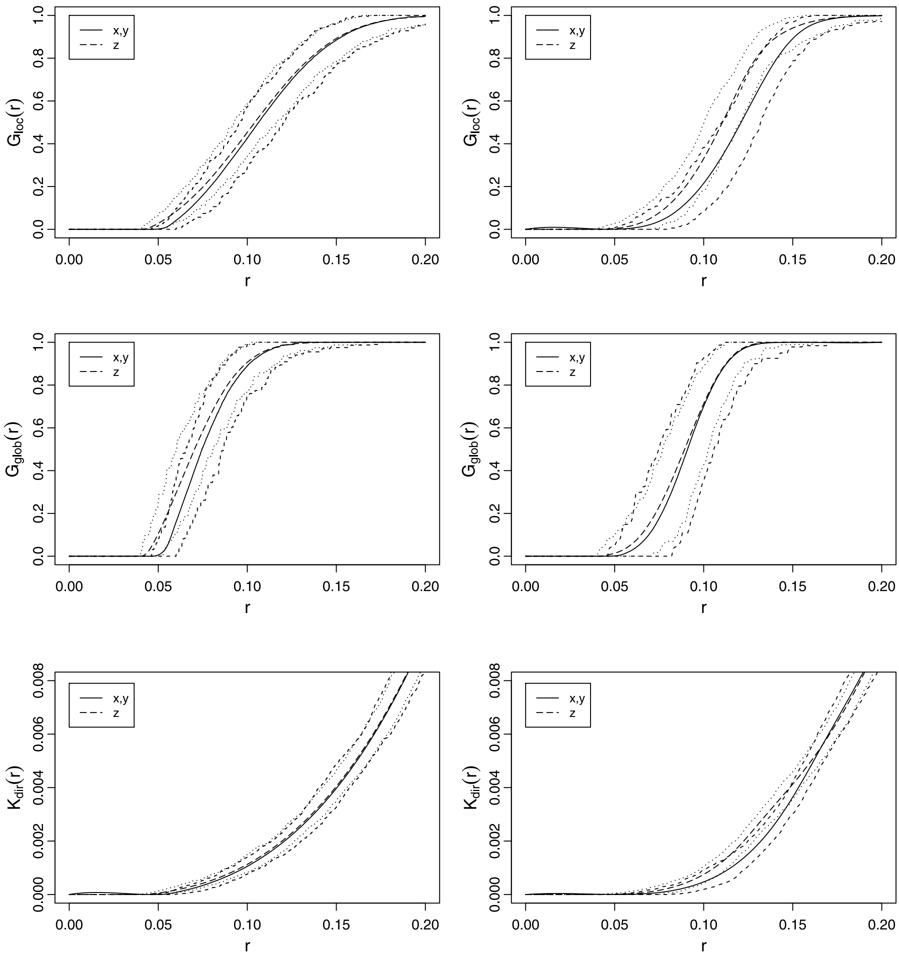

Fig. 1 Means (*solid* for xy, *dashed* for z) and envelopes (*short dashed* for xy, *dotted* for z) of the functions G_{loc}, G_{glob}, and K_{dir} (from *top* to *bottom*) evaluated for 1000 realizations of a pressed Matérn hard core point process (*left*) and a force biased packing (*right*) with parameters $\lambda = 500$ and $R = 0.05$. The pressing factor is $c = 0.8$

$[0, 1.1R]$. Comparing the powers for different summary statistics on this interval, we see that K_{dir} usually yields the best results. Only for $R = 0.025$ and $c = 0.9$, i.e., for the smallest hard core radius and the weakest pressing considered, it is one of the G functions which performs slightly better. Also, both G functions, especially G_{glob}, turn out to be more robust when changing the interval of observation. This can be explained by the fact that both functions are distribution functions which stabilize at a value of 1 for large values of r. The conjecture that tests based on summary statistics are superior to the test based on the eigenvalues of the orientation matrix is confirmed if the integration intervals for the summary statistics are chosen suitably.

The mean numbers of points contributing to the estimation of the G functions for the point patterns of intensity 500 are shown in Table 2. As expected, the numbers

Table 1 Powers in % of the isotropy tests on a 5% significance level for 1000 Matérn hard core point patterns of intensity $\lambda = 500$ and hard core radius R pressed by the factor c. The test statistics were computed on the interval $[0, r_2]$

$c \mid R$	0.025	0.025	0.025	0.05	0.05	0.05	0.075	0.075	0.075
$0.9 \mid r_2$	0.1	0.033	0.0275	0.1	0.067	0.055	0.2	0.1	0.0825
G_{loc}	**1.4**	6.6	26.6	3.7	23.2	77.9	18.0	65.7	98.9
G_{glob}	0.6	6.1	**26.8**	**4.8**	22.3	73.9	**39.1**	56.6	87.0
K_{dir}	1.0	**7.0**	26.7	4.5	**26.7**	**82.6**	7.9	**78.0**	**99.7**
λ_1		8.0			11.4			45.1	
$0.8 \mid r_2$	0.1	0.033	0.0275	0.1	0.067	0.055	0.2	0.1	0.0825
G_{loc}	**1.4**	21.9	49.3	15.4	72.7	97.2	77.8	99.8	**100**
G_{glob}	1.0	21.2	48.0	**21.3**	68.2	96.6	**93.9**	98.6	**100**
K_{dir}	1.3	**23.3**	**49.9**	19.9	**79.7**	**98.8**	36.9	**100**	**100**
λ_1		7.7			21.4			95.4	
$0.7 \mid r_2$	0.1	0.033	0.0275	0.1	0.067	0.055	0.2	0.1	0.0825
G_{loc}	**1.9**	**37.9**	56.3	41.4	95.0	99.3	98.3	**100**	**100**
G_{glob}	**1.9**	36.1	56.2	**50.7**	91.6	98.1	**98.9**	99.7	**100**
K_{dir}	1.6	**37.9**	**57.7**	44.6	**98.1**	**99.6**	75.7	**100**	**100**
λ_1		7.6			39.3			99.9	

are much smaller for G_{glob} than for G_{loc}. When increasing the pressing factor, a decrease of the numbers for the x- and y-direction is observed, while the numbers for the z-direction increase. This tendency is more pronounced for G_{glob} than for G_{loc}. In extreme cases it might lead to instabilities in the estimation of G_{glob} and a failure of the test.

4.2 Random packing of balls

To study also point patterns with a higher degree of regularity, we generated realizations of random packings of balls within the unit cube using the force-biased algorithm (Bezrukov et al. 2001). This algorithm works with the concept of collective rearrangement. It starts with a fixed number of balls which are randomly placed inside a container. Overlaps are permitted in the initial configuration, but gradually reduced by shifting the balls and reducing their sizes. Throughout, the initial size distribution is preserved up to a scaling factor. Using this algorithm, dense packings of balls with arbitrary radius distributions may be generated.

Here, we are working with balls of equal size. Their radii were chosen as 0.025 and 0.05, yielding hard core radii of $R = 0.05$ and $R = 0.1$, respectively. For the distribution of the number of balls, we chose a Poisson distribution with parameter $\lambda = 500$. As in the Matérn case, 1000 realizations were considered, and the ball packings were scaled by the vector $(\frac{1}{\sqrt{c}}, \frac{1}{\sqrt{c}}, c)$ with $c = 0.7, 0.8$, and 0.9.

Table 2 Mean number of points used for the estimation of G_{loc} and G_{glob} for the point processes of intensity $\lambda = 500$ in the Matérn (M) and the force biased (FB) case

	R	c	$G_{\mathrm{loc},x}$	$G_{\mathrm{loc},y}$	$G_{\mathrm{loc},z}$	$G_{\mathrm{glob},x}$	$G_{\mathrm{glob},y}$	$G_{\mathrm{glob},z}$
M	0.025	0.9	290.14	289.76	290.68	93.26	92.50	94.16
M	0.025	0.8	289.96	289.55	290.94	92.84	92.09	94.86
M	0.025	0.7	289.82	289.37	291.21	92.38	91.75	95.55
M	0.05	0.9	283.91	283.56	286.12	85.83	85.52	93.96
M	0.05	0.8	283.10	282.74	287.85	83.18	83.00	99.11
M	0.05	0.7	282.04	281.71	289.27	80.42	80.41	103.83
M	0.075	0.9	271.13	271.01	277.39	71.44	71.89	97.02
M	0.075	0.8	269.20	269.17	281.92	63.93	64.49	112.36
M	0.075	0.7	267.48	267.60	286.46	57.92	58.53	124.95
FB	0.05	0.9	267.06	266.84	270.01	72.49	72.97	91.84
FB	0.05	0.8	264.00	264.00	269.93	65.46	65.13	106.26
FB	0.05	0.7	259.83	259.34	267.10	57.70	57.09	120.20
FB	0.1	0.9	241.02	240.70	251.77	32.05	31.85	131.57
FB	0.1	0.8	237.64	237.37	258.71	12.81	12.78	183.13
FB	0.1	0.7	234.22	233.89	262.03	9.34	9.55	197.79

The envelopes of the directional summary statistics obtained for $R = 0.05$ are also shown in Fig. 1. Compared to the Matérn envelopes which are separated only close to the hard core radius, the difference between the curves for xy and z for K_{dir} and G_{loc} is more pronouned. For the larger hard core distance, the envelopes, which are not shown here, are even clearly disjoint over the whole interval of observation. Contrary, for G_{glob} they are closer together which is due to the small number of points included in the statistics in this case (see Table 2). This suggests to work with K_{dir} or G_{loc} and to choose larger intervals for the anisotropy tests when working with more regular data.

The test results in Table 3 confirm this impression. The highest powers are obtained for K_{dir} followed by G_{loc} if both are evaluated on the intermediate interval. For $R = 0.1$, we observe powers of 100% for the anisotropy tests based on G_{loc} and K_{dir} for suitably large intervals. In contrast, the test based on G_{glob} yields only poor results.

4.3 Existence of outliers

The results presented so far indicate that the range of observation for the directional summary statistics should be chosen depending on both the degree of regularity and the hard core distance observed in a particular point pattern. A situation which is likely to appear in real data is the existence of outliers, i.e., few points in the pattern are permitted to violate the hard core condition.

In order to study the behavior of the directional summary statistics in such cases, we insert outliers in some of the simulated point patterns and repeat the analyses

Table 3 Powers in % of the isotropy tests using directional summary statistics on a 5% significance level for 1000 force biased packings of intensity $\lambda = 500$ and ball radius R pressed by the factor c. The test statistics were computed on the interval $[0, r_2]$

$c \mid R$	0.05	0.05	0.05	0.1	0.1	0.1
$0.9 \mid r_2$	0.2	0.15	0.1	0.2	0.15	0.1
G_{loc}	**23.4**	27.1	14.9	**100**	**100**	51.4
G_{glob}	1.6	1.6	2.0	1.1	1.1	35.5
K_{dir}	13.4	**49.2**	**15.8**	**100**	**100**	**64.0**
$0.8 \mid r_2$	0.2	0.15	0.1	0.2	0.15	0.1
G_{loc}	85.2	87.0	63.8	**100**	**100**	97.3
G_{glob}	1.5	1.5	3.2	3.2	3.2	26.0
K_{dir}	**88.5**	**98.8**	**75.7**	**100**	**100**	**98.3**
$0.7 \mid r_2$	0.2	0.15	0.1	0.2	0.15	0.1
G_{loc}	99.2	99.5	97.3	**100**	**100**	**100**
G_{glob}	2.7	2.8	4.9	33.7	33.7	63.8
K_{dir}	**99.4**	**99.9**	**99.1**	**100**	**100**	**100**

described above. For that purpose, five points $x_1, \dots, x_5$ are chosen randomly from each point pattern. For each such point, an additional point y_i is generated from a uniform distribution on a ball of radius R centered in x_i. Then the directional summary statistics are estimated for the point patterns including the points $y_1, \dots, y_5$. To keep the amount of simulations limited, the analysis is restricted to patterns of intensity $\lambda = 500$.

The envelopes obtained for the Matérn hard core processes and the force-biased packings with $R = 0.05$ are shown in Fig. 2. In the Matérn case, the envelopes for the (x, y)- and the z-direction are no longer separated. Even in the pure hard core case this was only the case for values of r close to the hard core distance, exactly in the area which is most affected by the existence of outliers. The curves for the force-biased packings show similar changes for values close to R. Nevertheless, we might still expect acceptable power of the tests, since the results in the previous section suggested to use larger intervals in this case. The most striking changes are visible in the envelopes for G_{glob}, which is strongly influenced by the existence of outliers.

The powers of the isotropy tests are given in Tables 4 and 5. From the observation of the envelopes decreasing powers can be expected in the presence of outliers. Especially for G_{glob}, this indeed turns out to be the case. Besides this decrease, the results for the larger hard core radius $R = 0.075$ look similar to the results in the pure hard core case. On the interval $[0, 0.2]$ the G functions yield better results, while on both other intervals and in the total, K_{dir} performs best. For the smaller hard core radius $R = 0.05$, the situation is different. Now the best results for each of the functions are obtained using the intermediate interval since the structure of the curves for r close to the hard core radius R is mainly governed by the outliers. Again, the test based on K_{dir} yields the best total value.

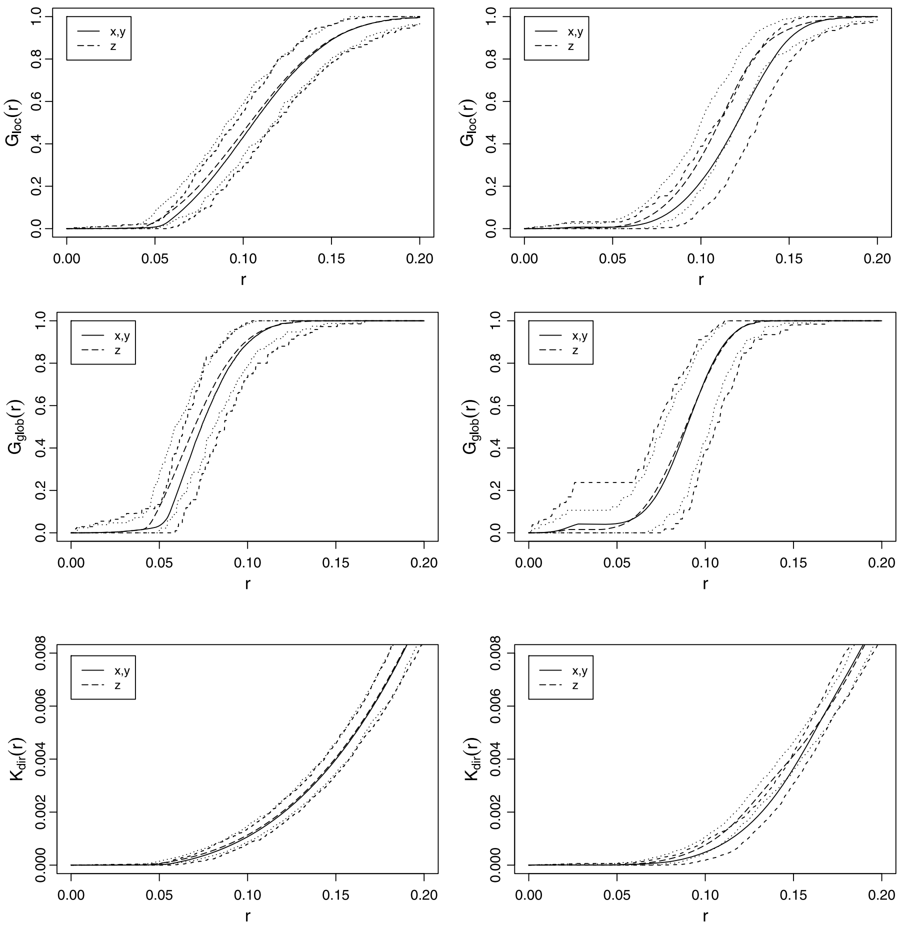

Fig. 2 Means (*solid* for xy, *dashed* for z) and envelopes (*short dashed* for xy, *dotted* for z) of the functions G_{loc}, G_{glob}, and K_{dir} (from *top* to *bottom*) evaluated for 1000 realizations of pressed Matérn hard core point processes (*left*) and force-biased packings (*right*) of intensity $\lambda = 500$ with five outliers. The hard core radius is $R = 0.05$, the pressing factor is $c = 0.8$

In the force-biased case the powers behave as expected, too. At least on the two larger intervals we obtain similar values as in the nonoutlier case.

5 Estimation of the pressing factor

We have seen that the anisotropy tests work well if both the intensity of the point pattern and the hard core radius are sufficiently large. Now we are going to investigate whether the statistics can also be used for the estimation of the pressing parameter c. For that purpose, we simulate 100 realizations of Matérn hard core point processes and force-biased packings with parameters as in Sect. 4. Each realization is pressed using the pressing factors $c = 0.7$, 0.8, 0.9, and 1.0. Then, every pattern is rescaled by

Table 4 Powers in % of the isotropy tests using directional summary statistics on a 5% significance level for 1000 Matérn hard core point patterns of intensity $\lambda = 500$ and hard core radius R including five outliers and pressed by the factor c. The test statistics were computed on the interval $[0, r_2]$

$c \mid R$	0.05	0.05	0.05	0.075	0.075	0.075
$0.9 \mid r_2$	0.1	0.067	0.055	0.2	0.1	0.0825
G_{loc}	2.8	10.4	**6.7**	14.1	56.2	81.8
G_{glob}	**3.9**	6.4	2.4	**23.1**	29.5	25.4
K_{dir}	3.3	**10.6**	5.0	6.0	**63.8**	**87.8**
$0.8 \mid r_2$	0.1	0.067	0.055	0.2	0.1	0.0825
G_{loc}	**13.7**	49.6	**45.1**	67.2	98.1	**100**
G_{glob}	**13.7**	30.6	17.2	**75.3**	84.3	79.3
K_{dir}	11.1	**54.3**	39.5	22.6	**99.4**	**100**
$0.7 \mid r_2$	0.1	0.067	0.055	0.2	0.1	0.0825
G_{loc}	**34.5**	77.8	68.3	**96.1**	**100**	**100**
G_{glob}	29.8	57.1	35.0	93.3	95.3	90.2
K_{dir}	33.4	**81.7**	**70.1**	65.1	**100**	**100**

Table 5 Powers in % of the isotropy tests using directional summary statistics on a 5% significance level for 1000 force-biased packings of intensity $\lambda = 500$ and hard core radius R including five outliers and pressed by the factor c. The test statistics were computed on the interval $[0, r_2]$

$c \mid R$	0.05	0.05	0.05	0.1	0.1	0.1
$0.9 \mid r_2$	0.2	0.15	0.1	0.2	0.15	0.1
G_{loc}	**23.9**	26.1	9.2	**100**	**100**	0.5
G_{glob}	0.5	0.5	0.6	0.1	0.1	0.1
K_{dir}	11.0	**44.2**	**9.6**	**100**	**100**	**0.6**
$0.8 \mid r_2$	0.2	0.15	0.1	0.2	0.15	0.1
G_{loc}	**82.2**	84.7	50.9	**100**	**100**	0.8
G_{glob}	0.0	0.0	0.0	0.1	0.1	0.1
K_{dir}	81.4	**97.9**	**58.5**	**100**	**100**	**1.3**
$0.7 \mid r_2$	0.2	0.15	0.1	0.2	0.15	0.1
G_{loc}	**98.9**	**99.0**	93.4	**100**	**100**	64.8
G_{glob}	0.1	0.1	0.1	0.0	0.0	0.1
K_{dir}	98.5	**99.0**	**97.6**	**100**	**100**	**96.7**

the vector $(\sqrt{d}, \sqrt{d}, \frac{1}{d})$, where d takes values between 0.6 and 1.1 at steps of 0.025. If the values of c and d are similar, both operations cancel out, and the resulting pattern is close to the original, hence isotropic. For large differences between c and d, however, the resulting pattern will show a certain degree of anisotropy which can be detected by our methods.

For each of the rescaled patterns, we compute the statistic $T_{\sum,d}$ (the statistic $T_{\sum}$ for the pattern rescaled by the factor d) based on all three summary statistics introduced above using two different choices of the integration interval: $[0, 1.1R]$ and $[0, \frac{4R}{3}]$ in the Matérn case and $[0, 0.15]$ and $[0, 0.2]$ for the force-biased packings. The statistic $T_{\sum}$ was chosen here rather than a statistic based on T_z or T_{xy}, since it allows for a simultaneous measurement of the deviation between all three directions. Now $\hat{c} = \operatorname{argmin}_d T_{\sum,d}$, i.e., the value of d leading to the most isotropic patterns, is considered as estimator for the pressing factor c.

The means of the estimated values and the mean squared error (MSE) of the estimation are displayed in Tables 6 and 7. Only the values for the interval yielding the smaller MSE are shown. In most of the cases, this turned out to be the smaller interval. In general, the trends observed in the testing part are confirmed in this study. The MSE for the estimates is smaller for higher intensities and higher degrees of regularity, and in most of the cases K_{dir} yields the best results. Only in some of the Matérn examples the degree of compression does not influence the estimation results as significantly as in the testing part. When interpreting the results one should keep in mind that the MSE is also influenced by the choice of the d values considered.

6 Application to the ice data

We now apply our estimation methods to ice samples from an ice core which was drilled during an ongoing deep drilling project at Talos Dome, Antarctica (159°04′ E, 72°46′ S). The achieved drilling depth after the season 2006/2007 is about 1600 m, only slightly less than the predicted absolute ice thickness. The accumulation rate is estimated to about 100 mm water equivalent per year in the Thalos Dome region (Stenni et al. 2002).

Three different depths between the firn–ice transition and the transition of bubbly to clathrate ice are chosen: 153 m, 353 m, and 505 m depth. For each depth, 14 samples are prepared to cover the structural variations on the centimeter scale as the amount of bubbles per volume ice is fluctuating on the small scale. The fluctuations correspond to variations in grain size at the firn–ice transition caused by seasonal variations in surface snow properties and snow fall events.

The samples are imaged by X-ray microfocus computer tomography (μCT) using a μCT-1072 (Skyscan, Belgium) inside a cold room at −15°C. The sample size is limited to cylinders of 15 mm diameter and 15 mm height. Therefore the ice is cut into cubes of 2 cm side length and rasped on a rotating turn table to form regular cylinders. The scanning volume is adjusted to the specific sample size by varying the spatial resolution between 13 and 16 μm per pixel. For each sample, a digital reconstruction algorithm generates a set of 900 images of 1024 × 1024 pixels.

In this paper, we restrict attention to the samples taken from 353 m and 505 m depth. Due to the large difference in X-ray absorption between air and ice, the volume images are simply segmented by global thresholding to identify air bubbles in the ice matrix (see Fig. 3). A subsequent labeling algorithm allows us to distinct the

Table 6 Means of the estimated pressing factors $\hat{c}_K$, $\hat{c}_{G_{\mathrm{loc}}}$, and $\hat{c}_{G_{\mathrm{glob}}}$ for the Matérn point patterns and MSE of the estimation

λ	R	r_2	c	$\bar{\hat{c}}_{\mathrm{loc}}$	MSE	$\bar{\hat{c}}_{\mathrm{glob}}$	MSE	$\bar{\hat{c}}_K$	MSE
1000	0.05	0.055	1.0	0.9988	5.813e−4	0.9995	7.625e−4	0.9993	**4.063e−4**
1000	0.05	0.055	0.9	0.8985	4.375e−4	0.8985	4.750e−4	0.8988	**3.438e−4**
1000	0.05	0.055	0.8	0.7988	**3.438e−4**	0.8018	5.313e−4	0.7990	4.125e−4
1000	0.05	0.055	0.7	0.6993	4.313e−4	0.6990	4.125e−4	0.6998	**3.938e−4**
1000	0.025	0.033	1.0	0.9480	1.513e−2	0.9513	1.596e−2	0.9590	**1.154e−2**
1000	0.025	0.033	0.9	0.8745	1.335e−2	0.8858	**1.071e−2**	0.8950	1.270e−2
1000	0.025	0.033	0.8	0.8248	**1.141e−2**	0.8250	1.360e−2	0.8285	1.290e−2
1000	0.025	0.0275	0.7	0.6865	7.325e−3	0.6820	7.038e−3	0.6923	**6.769e−3**
500	0.075	0.0825	1.0	1.0000	5.625e−4	1.0000	5.375e−4	0.9988	**5.063e−4**
500	0.075	0.0825	0.9	0.8955	5.250e−4	0.8968	7.438e−4	0.8973	**4.563e−4**
500	0.075	0.0825	0.8	0.7973	4.438e−4	0.7945	9.625e−4	0.7980	**4.375e−4**
500	0.075	0.0825	0.7	0.6978	5.063e−4	0.7003	5.813e−4	0.6963	**4.813e−4**
500	0.05	0.055	1.0	0.9828	**3.944e−3**	0.9795	6.763e−3	0.9875	4.850e−3
500	0.05	0.055	0.9	0.8810	5.813e−3	0.8855	5.138e−3	0.8933	**3.631e−3**
500	0.05	0.055	0.8	0.7780	5.363e−3	0.7818	4.544e−3	0.7923	**2.844e−3**
500	0.05	0.055	0.7	0.6880	**1.850e−3**	0.6913	1.981e−3	0.6860	1.988e−3
500	0.025	0.033	1.0	0.8270	6.264e−2	0.8285	6.020e−2	0.8335	**5.733e−2**
500	0.025	0.033	0.9	0.8158	3.473e−2	0.8210	**3.291e−2**	0.8200	3.335e−2
500	0.025	0.033	0.8	0.7678	2.299e−2	0.7860	2.364e−2	0.7708	**2.037e−2**
500	0.025	0.0275	0.7	0.6263	9.981e−3	0.6245	**9.663e−3**	0.6263	1.00e−2

single bubbles and to compute their centers. For the estimation of the summary statistics, cuboidal observation windows are fitted into the cylinders, and all pore centers contained in the cuboids are extracted. In order to find the maximal number of pores for each sample, the observation windows are not required to have equal size. Only objects with a volume larger than 25 voxels are included in the analysis yielding point patterns containing between 329 and 733 points. All image processing steps are performed on volume images using the MAVI software package (Fraunhofer ITWM 2005). Figure 4 shows visualizations of one sample from each depth.

In contrast to the simulated data, the pore intensities in different ice samples cannot be assumed to be the same due to the variations on the centimeter scale. Therefore, we use the ratio estimation method described in Baddeley et al. (1993) to pool the summary statistics within the depths. This means that the mean curves are estimated as

$$\hat{S} = \frac{\sum_{i=1}^{14} U_i}{\sum_{i=1}^{14} V_i}.$$

For K_{dir}, U_i is the double sum in (1), and V_i is the estimated squared intensity evaluated for sample i. For the G functions, U_i and V_i are the numerators and denomina-

Table 7 Means of the estimated pressing factors $\hat{c}_K$, $\hat{c}_{G_{\text{loc}}}$, and $\hat{c}_{G_{\text{glob}}}$ for force-biased packings with m outliers and MSE of the estimation

λ	R	m	r_2	c	$\bar{\hat{c}}_{\text{loc}}$	MSE	$\bar{\hat{c}}_{\text{glob}}$	MSE	$\bar{\hat{c}}_K$	MSE
500	0.1	0	0.15	1.0	1.0005	2.000e−4	1.0130	4.200e−3	0.9983	**1.063e−4**
500	0.1	0	0.15	0.9	0.8998	1.438e−4	0.9290	5.763e−3	0.8985	**7.500e−5**
500	0.1	0	0.15	0.8	0.7995	1.000e−4	0.8378	7.806e−3	0.7990	**6.250e−5**
500	0.1	0	0.15	0.7	0.6998	4.375e−5	0.7358	8.419e−3	0.6995	**1.250e−5**
500	0.1	5	0.15	1.0	0.9988	1.938e−4	1.0103	3.806e−3	0.9980	**1.125e−4**
500	0.1	5	0.15	0.9	0.8988	1.563e−4	0.9320	6.150e−3	0.8990	**6.250e−5**
500	0.1	5	0.15	0.8	0.7990	1.250e−4	0.8470	1.095e−2	0.7993	**3.125e−5**
500	0.1	5	0.15	0.7	0.6993	4.375e−5	0.7660	1.805e−2	0.6995	**2.500e−5**
500	0.05	0	0.15	1.0	1.0005	2.625e−3	0.9385	2.081e−2	0.9955	**1.813e−3**
500	0.05	0	0.15	0.9	0.8953	2.806e−3	0.9060	1.819e−2	0.8993	**1.669e−3**
500	0.05	0	0.15	0.8	0.7968	2.306e−3	0.8655	2.511e−2	0.8030	**1.013e−3**
500	0.05	0	0.15	0.7	0.6958	1.631e−3	0.8128	3.222e−2	0.7015	**7.125e−4**
500	0.05	5	0.15	1.0	0.9920	3.163e−3	0.9195	2.649e−2	1.0018	**1.819e−3**
500	0.05	5	0.15	0.9	0.9023	3.294e−3	0.8705	2.038e−2	0.9025	**1.775e−3**
500	0.05	5	0.15	0.8	0.8033	2.594e−3	0.8745	3.070e−2	0.8043	**1.444e−3**
500	0.05	5	0.15	0.7	0.6995	2.088e−3	0.8188	3.722e−2	0.6990	**1.013e−3**

tors, respectively, in (2) and (3). Scatter plots of U_i against V_i, which are not shown here, indicated that the assumption of a linear relation between these numbers is justified. The means and envelopes given by the minima and maxima of the observed values of the directional summary statistics G_{loc} and K_{dir} for the ice samples are shown in Fig. 5. Especially for K_{dir}, a clear deviation between the envelopes for the (x, y)- and the z-directions is observed. Therefore, the hypothesis of isotropy can clearly be rejected in this case.

For the estimation of the pressing factors, we have to choose a suitable interval of integration. Therefore, we first investigate the degree of regularity of the pore system by estimating the pair-correlation function of the point patterns of pore centers. Although the point patterns we are dealing with are clearly anisotropic, we believe that the isotropic pair-correlation function, which is easy to estimate, is sufficient for this purpose. The results for five samples from each depth are shown in Fig. 6. The wave-like appearance of the curves resembles the structure which is typically observed in pair-correlation functions of dense packings of balls (Stoyan et al. 1995). This is an evidence for a very regular structure of the data.

The histograms of the nearest-neighbor distances for three samples per depth are shown in Fig. 7. The gaps on the left tail of the histograms indicate the existence of outliers in the ice samples.

Combined with the results of our simulation studies, these observations suggest the choice of an intermediate interval size for the estimation of the pressing factors and the use of G_{loc} or K_{dir} rather than G_{glob}. The overlap of the envelopes shown in Fig. 5 is small over the whole interval [0, 2.0]. Therefore, we decided to choose [0, 2.0] for

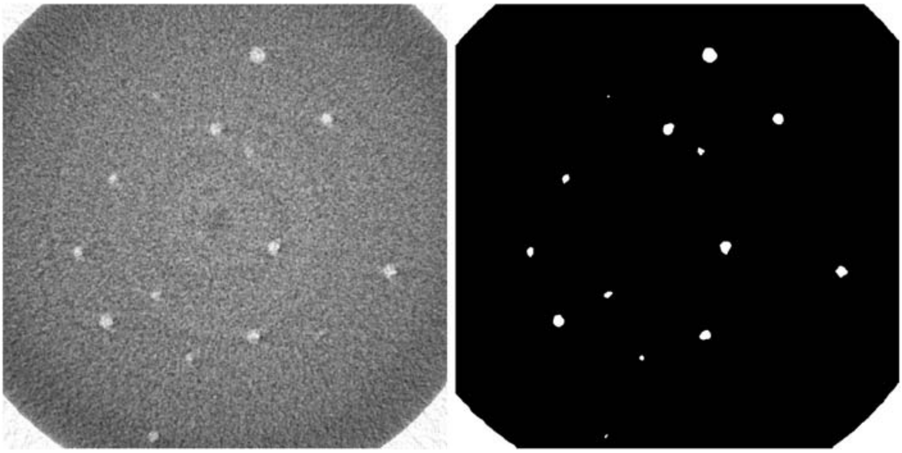

Fig. 3 2D sections of the original (*left*) and the binarized (*right*) image of an ice sample from depth 353 m

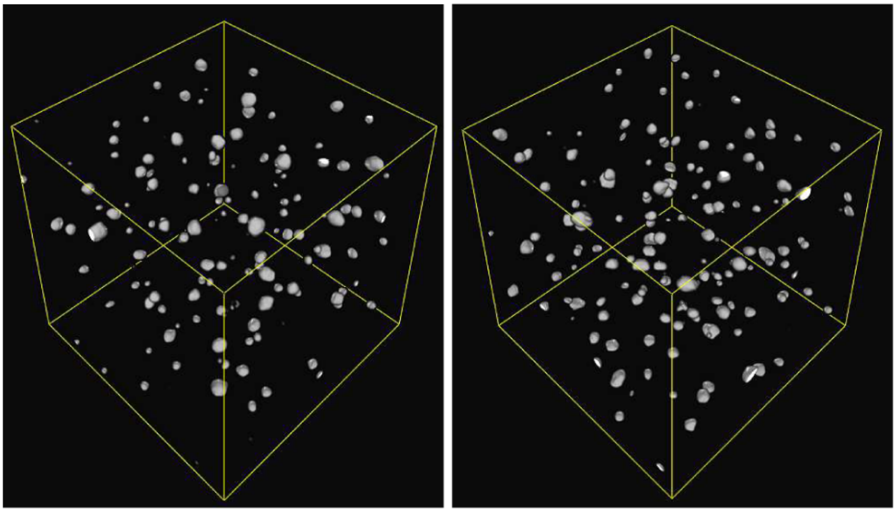

Fig. 4 Visualizations of the system of air pores in ice samples from depth 353 m (*left*) and 505 m (*right*)

the estimation of the pressing factors, which allows us to control the behavior of the functions over the whole range. For the rescaling of the samples from depth 353 m, we used values of d ranging between 0.5 and 1.0 at steps of 0.025. Since stronger pressing is expected in deeper areas, the values for the samples from depth 505 m were chosen between 0.3 and 0.8. The estimates $\hat{c}_G$ and $\hat{c}_K$ obtained using G_{loc} and K_{dir} are given in Table 8. They confirm that the compression of the ice is stronger at the depth 505 m than at 353 m depth.

In order to investigate the estimation variance in this case, we adopt a bootstrap method as described in Illian et al. (2008, p. 454). For each of the two summary statistics and depths, 200 new samples of $\hat{c}$ values are generated by random resampling

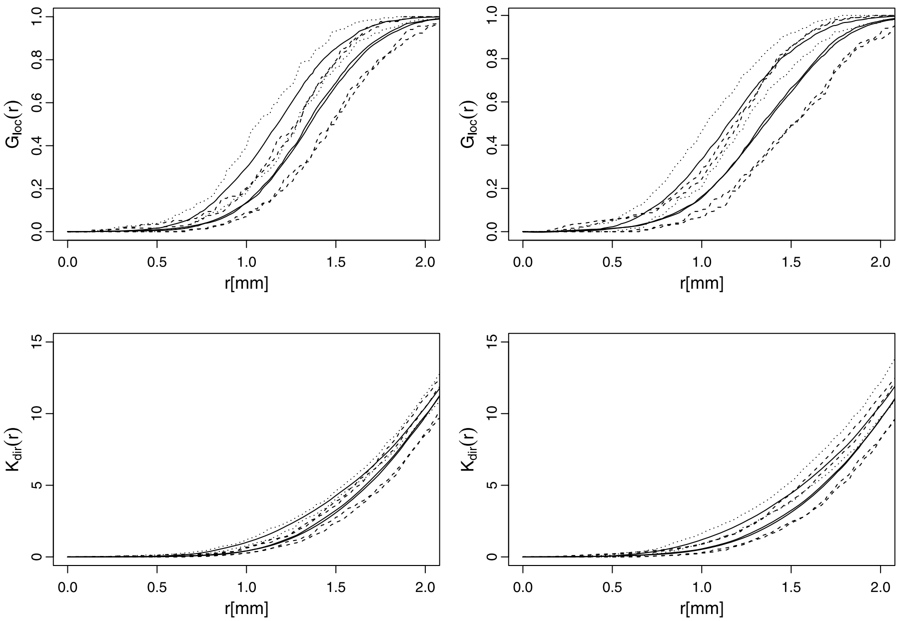

Fig. 5 Means (*solid*) and envelopes (*short dashed* for x and y, *dotted* for z) of the functions G_{loc} (*top*) and K_{dir} (*bottom*) evaluated for the ice samples from depth 353 m (*left*) and 505 m (*right*)

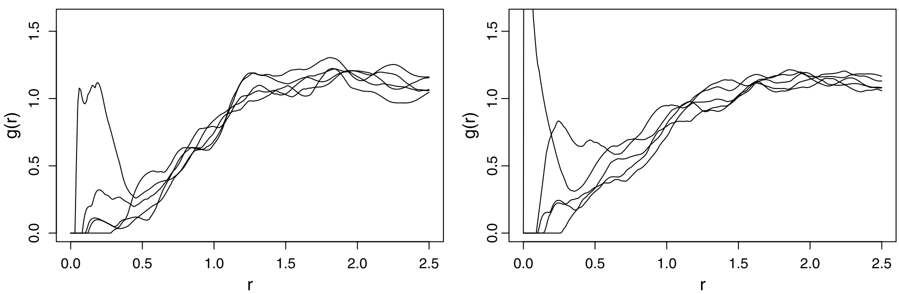

Fig. 6 Isotropic pair correlation functions estimated for five ice samples taken from depth 353 m (*left*) and 505 m (*right*)

from the estimated values with replacement. The estimation variance is then approximated by the sample variance of their means. For depth 353 m, we obtained values of $3.045 \cdot 10^{-4}$ (G_{loc}) and $1.667 \cdot 10^{-4}$ (K_{dir}), the values for 505 m are $9.341 \cdot 10^{-5}$ (G_{loc}) and $2.543 \cdot 10^{-4}$ (K_{dir}). The corresponding 95% confidence intervals are disjoint for the two depths considered. They are

$$353\text{ m:}\quad (0.607, 0.679) \text{ using } G_{\mathrm{loc}} \quad \text{and} \quad (0.604, 0.655) \text{ using } K_{\mathrm{dir}}, \quad \text{and}$$

$$505\text{ m:}\quad (0.518, 0.577) \text{ using } G_{\mathrm{loc}} \quad \text{and} \quad (0.516, 0.552) \text{ using } K_{\mathrm{dir}}.$$

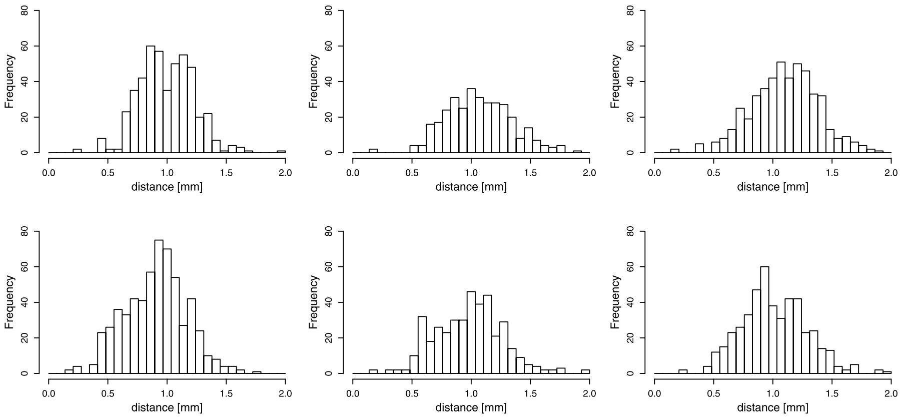

Fig. 7 Histograms of distances to the nearest neighbors for three samples from depth 353 m (*top*) and 505 m (*bottom*)

Table 8 Results for the ice samples: number of pores n, pores per volume N_V, and the pressing factors $\hat{c}_G$ and $\hat{c}_K$ estimated using G_{loc} and K_{dir}, respectively

353 m	n	N_V	$\hat{c}_G$	$\hat{c}_K$	505 m	n	N_V	$\hat{c}_G$	$\hat{c}_K$
1	411	0.3511	0.575	0.575	1	675	0.3559	0.500	0.575
2	431	0.3228	0.550	0.550	2	733	0.4414	0.550	0.500
3	398	0.2981	0.625	0.625	3	549	0.2937	0.500	0.700
4	478	0.3906	0.675	0.675	4	639	0.4310	0.550	0.525
5	411	0.4019	0.625	0.625	5	590	0.4398	0.500	0.625
6	439	0.3861	0.675	0.600	6	398	0.3063	0.500	0.500
7	372	0.3125	0.650	0.575	7	356	0.2682	0.550	0.525
8	334	0.2938	0.550	0.575	8	439	0.2761	0.575	0.500
9	369	0.3246	0.575	0.600	9	493	0.2969	0.600	0.525
10	329	0.3907	0.650	0.775	10	463	0.2870	0.500	0.475
11	550	0.3220	0.650	0.750	11	479	0.2885	0.500	0.550
12	485	0.2754	0.700	0.725	12	466	0.2931	0.575	0.575
13	649	0.3577	0.650	0.650	13	541	0.3357	0.575	0.575
14	711	0.3318	0.675	0.675	14	413	0.2715	0.500	0.475
Mean	454.79	0.3403	0.630	0.641	Mean	516.71	0.3241	0.534	0.545

In order to further evaluate the estimates, the mean curves of G_{loc} and K_{dir} for the rescaled point patterns from depth 353 m are shown in Fig. 8. For both functions, the difference between the (x, y)- and the z-directions turns out to be small in the rescaled patterns. The same is true for the samples from depth 505 m.

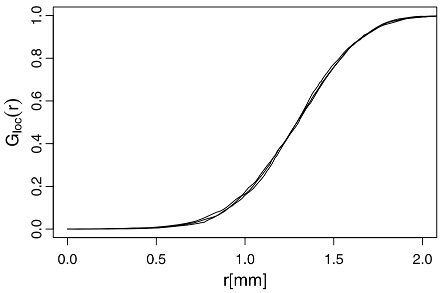

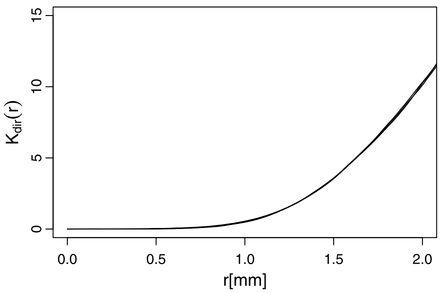

Fig. 8 Means of the functions G_{loc} and K_{dir} for the rescaled versions of the ice samples from depth 353 m using the estimated pressing factors $\hat{c}_G$ and $\hat{c}_K$, respectively

7 Discussion

The main aim of the paper was to study anisotropy of air pores in polar ice. The hypothesis is that the ice is compressed and therefore, the spatial pattern of the air pores in z-direction differs from the pattern in x- or y-direction. To investigate this, we introduced some directional summary statistics in 3D based on the nearest-neighbor distance distribution function and Ripley's K function. These summary statistics were used to develop tests for isotropy against this specific type of anisotropy. An adaptation of the methods for the detection of anisotropies with respect to other directions is straightforward.

The tests presented here are based on replicates and have the advantage that there is no need to assume and fit a model to the data. In a simulation study we evaluated the powers of the tests for regular patterns of different intensities, degrees of regularity, and strengths of compression. As expected, the best results (highest powers) were obtained with high intensities, high degrees of regularity (e.g., large hard-core radii) and strong pressing. For Matérn hard core point processes, the test based on the directional K function performed best. The size of the interval of observation should be chosen depending on the hard core distance. However, it turned out that tests based on the G functions are more robust to changes of this interval. For point processes with a high degree of regularity, such as packings of balls, the use of the K function or the local G function on a larger interval is recommended. In this case, our methods also proved robust to the existence of outliers. In the point process literature it is often suggested to use more than one summary statistic for the analysis of a point pattern. Despite the better test results for K_{dir}, it seems therefore advisable to work with both K_{dir} and G_{loc}.

If only a few replicates are available, it is possible to perform a Monte Carlo test based on the summary statistics presented here. In this case, it is necessary to find an appropriate model for the data in order to be able to simulate patterns from it. The results based on the Monte Carlo test are similar to the results based on the data-based tests, when testing on simulated data. If the regularity in the data is not very pronounced, one has to be careful when determining the hard core distance, since it affects the choice of the interval on which the differences between the summary statistics in different directions are investigated.

In addition to the summary statistics we have considered here, the distribution of the distances not only to the nearest neighbor but to all other points in the pattern could be investigated. This function is closely related to the point-pair rose density. The advantage of using all points is discussed in a paper by Fry (1979) on strain measurement in rocks. For the estimation of this function, only distances up to a maximal value should be considered. Depending on how large this value is chosen, an edge correction similar to the ones for the G functions would result in estimates based on either a small number of points with a lot of information or a large number of points with little information. It is not clear in advance which alternative should be preferred.

We performed a simulation study for regular patterns with hard core since the air pore patterns are regular. However, it is also interesting to investigate how the tests work for clustered patterns. In this case, the aim is a detection of a change of the shapes of clusters caused by the pressing. We performed a simulation study also for Matérn cluster processes even though the results are not reported here. As in the hard core case, both high intensities and large pressing factors yield high powers of the test. In contrast to the regular case, anisotropies within point patterns with small cluster radii are easier to detect than within patterns with large cluster radii, since the concentration of points within the clusters is higher. Also, it turns out that the tests work better in the case of less points in a cluster. As in the regular case, the test based on the K function works best followed by the local G function, while the global G function yields only poor results.

For the analysis of the ice samples, not only the detection of anisotropies was required but also the measurement of its strength. In order to study this, we introduced a method to estimate the pressing factor. The observed pattern is "stretched" using different pressing factors. The factor minimizing the difference between the spatial structure in the three coordinate directions, hence yielding the most isotropic pattern, is chosen as the estimate of the pressing factor. The evaluation of the estimation procedure on simulated data produced satisfactory results. Especially for very regular patterns, the method works very well even in the presence of outliers.

Applied to the ice data, our methods render the anisotropy in z-direction caused by the compression of the ice sheet clearly visible. The means of the estimated pressing factors of $0.63/0.64$ for the samples from 353 m depth and $0.53/0.55$ for the depth of 505 m are consistent with the expected increase of the degree of compression with increasing depth. For the samples from 153 m depth, we obtained mean pressing factors of $0.81/0.82$ which confirms this finding. However, the comparison of the mean curves for the two depths shown in Fig. 9 indicate further structural differences between samples from different depths. A detailed investigation of these questions including samples from further depths is subject to future research.

A simple model of ice flow known as Nye formula in the glaciological literature (described in Paterson 1994) assumes a constant thinning rate with depth. The Nye-approach is fairly simple and needs only the absolute ice thickness as an input parameter. Assuming an ice thickness of about 1600 m for Talos Dome, one gets thinning factors of 0.90 (153 m), 0.78 (353 m), and 0.68 (505 m). Our estimations show an excellent agreement in the relative trend but with an absolute offset of about 0.1. One possible reason might be the oversimplification of the Nye-approach. It takes

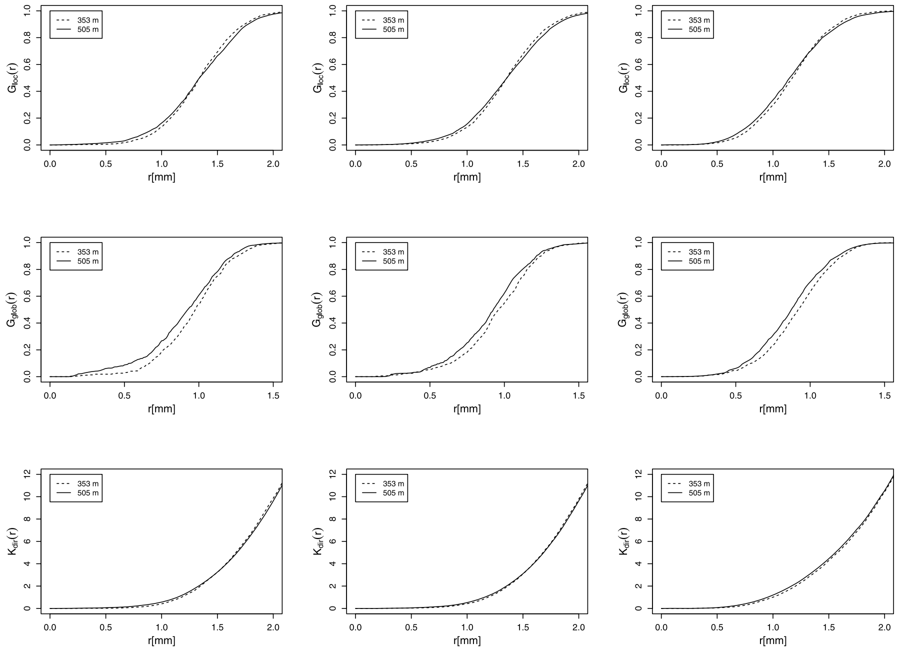

Fig. 9 Comparison of the directional summary statistics for the ice samples from depths 353 m and 505 m. Means of the functions G_{loc}, G_{glob}, and K_{dir} (from *top* to *bottom*) evaluated for the x-, y-, and z-directions (from *left* to *right*)

neither the bedrock boundary conditions nor the change of mechanical properties of ice with age and climate into account. The absolute thinning factor is very sensitive against the bedrock conditions. An assumed freezing at the bedrock would shift the absolute values in the upper part of the ice sheet towards higher thinning factors. Simulations with the so called Dansgaard–Johnsen approach (also described in Paterson 1994) which parameterized the effect of bedrock freezing with a linear decrease of the thinning rate to zero at bedrock results in absolute thinning factors comparable to our estimations. However, the parameterization of the linear decrease is arbitrary in the model, and the real bedrock conditions at the Talos Dome site are not known due to the incomplete drilling so far. However, the qualitative agreement with the pure constrained model representations gives us confidence that the dating of ice cores will benefit from the independent estimations of the thinning function in future.

Acknowledgements We would like to thank Björn Wagner for assistance with the image processing. Claudia Redenbach and Aila Särkkä acknowledge support by the Swedish Foundation for Strategic Research (SSF) through the Gothenburg Mathematical Modelling Centre (GMMC).

References

Anderson, T.W., Stephens, M.A.: Tests for randomness of directions against equatorial and bimodal alternatives. Biometrika **59**(3), 613–621 (1972)

Baddeley, A.J., Moyeed, R.A., Howard, C., Boyde, A.: Analysis of a three-dimensional point pattern with replication. Appl. Stat. **42**, 641–668 (1993)

Bender, M., Sowers, T., Dickson, M.L., Orchardo, J., Grootes, P., Mayewski, P.A., Meese, D.A.: Climate correlations between Greenland and Antarctica during the past 100 000 years. Nature **372**, 663–666 (1994)

Bezrukov, A., Bargiel, M., Stoyan, D.: Statistical analysis of simulated random packings of spheres. Part. Part. Syst. Charact. **19**, 111–118 (2001)

Diggle, P.: Statistical Analysis of Spatial Point Patterns. Academic Press, San Diego (2003)

Duval, P.: Deformation and dynamic recrystallization of ice in polar ice sheets. In: Hondoh, T. (ed.) Physics of Ice Core Records. Hokkaido University Press, Sapporo (2000)

EPICA community members: Eight glacial cycles from an antarctic ice core. Nature **429**, 623–628 (2004)

EPICA community members: One-to-one coupling of glacial climate variability in Greenland and Antarctica. Nature **444**, 195–198 (2006)

Fraunhofer ITWM: MAVI—Modular Algorithms for Volume Images (2005). http://www.itwm.fhg.de/mab/projects/MAVI

Fry, N.: Random point distributions and strain measurement in rocks. Tectonophysics **60**, 89–105 (1979)

Hanisch, K.H.: Some remarks on estimators of the distribution function of nearest neighbour distance in stationary spatial point processes. Math. Oper. Stat. Ser. Stat. **15**(3), 409–412 (1984)

Illian, J., Penttinen, A., Stoyan, H., Stoyan, D.: Statistical Analysis and Modelling of Spatial Point Patterns. Wiley, New York (2008)

Parrenin, F., Dreyfus, G., Durnad, G., Fujita, S., Gagliardini, O., Gilet, F., Jouzel, J., Kawamura, K., Lhomme, N., Masson-Delmotte, V., Ritz, C., Schwander, J., Shoji, H., Uemura, R., Watanabe, O., Yoshida, N.: 1-D-ice flow modelling at EPICA Dome C and Dome Fuji, East Antarctica. Clim. Past **3**, 243–259 (2007)

Paterson, W.S.B.: The Physics of Glaciers. Pergamon, Elmsford (1994)

Ruth, U., Barnola, J., Beer, J., Bigler, M., Blunier, T., Castellano, E., Fischer, H., Fundel, F., Huybrechts, P., Kaufmann, P., Kipfstuhl, S., Lambrecht, A., Morganti, A., Oerter, H., Parrenin, F., Rybak, O., Severi, M., Udisti, R., Wilhelms, F., Wolff, E.: EDML1: A chronology for the EPICA deep ice core from Dronning Maud Land, Antarctica, over the last 150 000 years. Clim. Past **3**, 475–484 (2007)

Severi, M., Becagli, S., Castellano, E., Morganti, A., Traversi, R., Udisti, R., Ruth, U., Fischer, H., Huybrechts, P., Wolff, E., Parrenin, F., Kaufmann, P., Lambert, F., Steffensen, J.P.: Synchronisation of the EDML and EDC ice cores for the last 52 kyr by volcanic signature matching. Clim. Past **3**, 367–374 (2007)

Stenni, B., Proposito, M., Gragnani, R., Flora, O., Jouzel, J., Falourd, S., Frezotti, M.: Eight centuries of volcanic signal and climate change at Talos Dome (East Antarctica). J. Geophys. Res. **107**(D9), 4076–4089 (2002)

Stoyan, D.: Describing the anisotropy of marked planar point processes. Statistics **22**, 449–462 (1991)

Stoyan, D., Beneš, V.: Anisotropy analysis for particle systems. J. Microsc. **164**, 159–168 (1991)

Stoyan, D., Stoyan, H.: Fractals, Random Shapes and Point Fields. Wiley, New York (1994)

Stoyan, D., Kendall, W.S., Mecke, J.: Stochastic Geometry and its Applications, 2nd edn. Wiley, New York (1995)